Journal of Inorganic Biochemistry 199 (2019) 110761

Contents lists available at ScienceDirect

Journal of Inorganic Biochemistry

journal homepage: www.elsevier.com/locate/jinorgbio

Redox thermodynamics of B-class dye-decolorizing peroxidases

Vera Pfanzagl[a], Marzia Bellei[b], Stefan Hofbauer[a], Christophe V.F.P. Laurent[c], Paul G. Furtmüller[a], Chris Oostenbrink[c], Gianantonio Battistuzzi[d], Christian Obinger[a,*]

[a] Department of Chemistry, Institute of Biochemistry, University of Natural Resources and Life Sciences, Vienna, Muthgasse 18, 1190 Vienna, Austria
[b] Department of Life Sciences, University of Modena and Reggio Emilia, via Campi 103, 41125 Modena, Italy
[c] Department of Material Science and Process Engineering, Institute of Molecular Modeling and Simulation, University of Natural Resources and Life Sciences, Vienna, Muthgasse 18, 1190 Vienna, Austria
[d] Department of Chemistry and Geology, University of Modena and Reggio Emilia, via Campi 103, 41125 Modena, Italy

ARTICLE INFO

Keywords:
Heme peroxidase
Dye-decolorizing peroxidase
Redox thermodynamics
Compound I
Spectroelectrochemistry
Molecular dynamics simulation

ABSTRACT

With > 5000 annotated genes dye-decolorizing peroxidases (DyPs) represent a heme *b* peroxidase family of broad functional diversity. Bacterial B-class DyPs are poor peroxidases of unknown physiological function. Hydrogen peroxide efficiently mediates the rapid formation of Compound I in B-class DyPs, which, however, is stable and shows modest reactivity towards organic and inorganic electron donors. To understand these characteristics, we have investigated the redox thermodynamics of the one-electron reduction of the ferric high-spin form of wild-type B-class DyP from the pathogenic bacterium *Klebsiella pneumoniae* (*Kp*DyP) and the variants D143A, R232A and D143A/R232A. These distal amino acids are fully conserved in all DyPs and play important roles in Compound I formation and maintenance of the heme cavity architecture and substrate access route(s). The $E^{\circ\prime}$ values of the respective redox couples Fe(III)/Fe(II) varied from −350 mV (wild-type *Kp*DyP) to −299 mV (D143A/R232A) at pH 7.0. Variable-temperature spectroelectrochemical experiments revealed that the reduction reaction of B-class DyPs is enthalpically unfavored but entropically favored with significant differences in enthalpic and entropic contributions to $E^{\circ\prime}$ between the four proteins. Molecular dynamics simulations demonstrated the impact of solvent reorganization on the entropy change during reduction reaction and revealed the dynamics and restriction of substrate access channels. Obtained data are discussed with respect to the poor peroxidase activities of B-class DyPs and compared with heme peroxidases from other (super)families as well as with chlorite dismutases, which do not react with hydrogen peroxide but share a similar fold and heme cavity architecture.

1. Introduction

In 1999, a novel heme-containing peroxidase was identified in the fungus *Bjerkandera adusta* (formerly *Geotrichum candidum*) [1]. This heme *b* oxidoreductase bore no homology to any known heme peroxidases with respect to enzymatic activity as well as overall and active site structure. It was named dye-decolorizing peroxidase (DyP) for its ability to efficiently catalyze the decolorization of bulky industrial dyes such as anthraquinone derivatives. Structural characterization of DyPs revealed the presence of a two-domain, α + β ferredoxin-like fold that is distinct from the α-helical fold of the other heme peroxidase superfamilies [2]. In all DyPs characterized to date, the heme has limited solvent access and binds to the larger C-terminal domain of the protein. The conserved residues include the proximal axial ligand histidine (H215 in B-class DyP from *Klebsiella pneumoniae*, *Kp*DyP), which is hydrogen bonded to the carboxylate of an acidic residue (D268 in *Kp*DyP). Three residues on the distal side are equally conserved in all DyPs, namely aspartate (D143), arginine (R232) and phenylalanine (F248) (Fig. 1) [3,4]. Arginine 232 forms a salt bridge with the propionate at position 7 (thereby stabilizing the distal architecture) and, together with D143 and F248, forms the bottleneck of the main access channel to the heme.

Phylogenetic analysis of DyPs shows three distinct phylogenetic classes, called A, B, and C/D, which differ in structure, oligomeric state, (predicted) localization and enzymatic activity [3]. Inconsistent with their denomination, not all classes of DyPs have reliable peroxidase activity, suggesting that this activity might not always be relevant to their physiological role. Especially for B-class DyPs the biological substrates are unknown and a broad functional diversity has been reported including deferrochelatase [5] or porphyrin oxidase [6] activities as

* Corresponding author.
E-mail address: christian.obinger@boku.ac.at (C. Obinger).

https://doi.org/10.1016/j.jinorgbio.2019.110761
Received 27 May 2019; Received in revised form 22 June 2019; Accepted 8 July 2019
Available online 11 July 2019

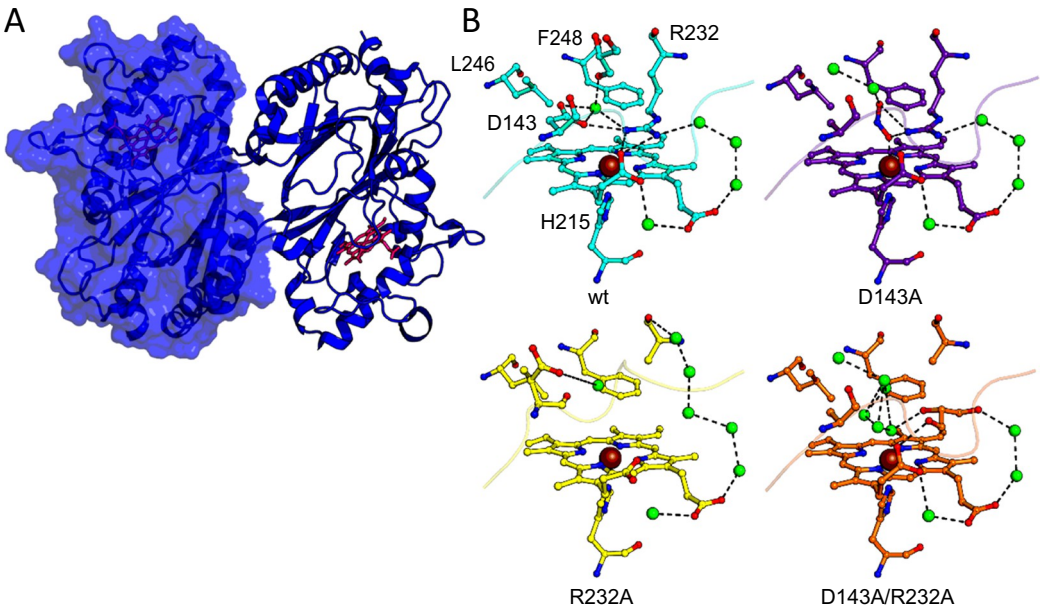

Fig. 1. Overall structure of dimeric wild-type dye-decolorizing peroxidase of *Klebsiella pneumoniae* (*Kp*DyP) and active site structures of the variants D143A, R232A, and D143A/R232A.
(A) Ribbon representation of the crystal structure of dimeric wild-type (wt) *Kp*DyP showing secondary structure elements (subunit A) and the protein surface (subunit B, semi-transparent). Each subunit contains a heme *b* cofactor depicted in pink. (B) Stick representation of the heme cavity of the variants D143A, R232A, L246A and D143A/R232A. The proximal ligand H215 and the distal amino acid residues lining the access channel bottleneck (D143, R232, L246 and F248) to the heme cofactor are shown (subunit A). Possible hydrogen bonds between conserved crystal waters (green spheres), active site ligands [NO_2^- in D143 (purple), glycerol in D143A/R232A (orange)] and amino acid residues are shown as dashed lines (black). The backbone of the outer loop surrounding the active site cavity is shown as a semitransparent ribbon. The figure was generated using the PyMOL Molecular Graphics System (version 1.7.0.0, Schrödinger, LLC). (For interpretation of the references to color in this figure legend, the reader is referred to the web version of this article.)

well as oxidative degradation of phenolic lignin-derived compounds [7]. Our recent data also challenge the idea that peroxidase activity towards conventional (aromatic) substrates is related to the physiological roles of B-class DyPs [4]. We have presented the high resolution crystal structures of wild-type *Kp*DyP and the variants D143A, R232A and D143A/R232A and demonstrated the role of D143 as proton acceptor in heterolytic cleavage of hydrogen peroxide and the formation of stable and poor oxidizing Compound I [i.e. an oxoiron(IV)porphyrin π-cation radical]. Elimination of distal R232 was shown to promote a collapse of the distal heme cavity including blocking of one access channel [4]. Furthermore, we demonstrated that (i) serotonin is able to reduce Compound I to Compound II albeit in a slow reaction, and that (ii) elimination of D143 significantly enhances the reactivity of Compound I towards both one- and two-electron donors [4].

In order to better understand these structure-function relationships of B-class DyPs, we have studied the temperature-dependence of the standard reduction potential, $E^{\circ\prime}$, of the Fe(III)/Fe(II) couple of wild-type *Kp*DyP and the variants D143A, R232A and D143A/R232A and determined the enthalpic and entropic contributions of the protein and the solvent to the reduction reaction of the Fe(III) high-spin forms of these proteins. Furthermore, molecular dynamics simulations of the ferric and ferrous states of the four proteins were performed in order to study the impact of exchange of D143 and/or R232 on the dynamics of conformation of the active site architecture and access routes to the heme cavity and on solvent reorganization during Fe(III) to Fe(II) reduction. The obtained data are discussed with respect to the role of distal D143 and R232 in controlling access to and reactivity of heme in *Kp*DyP. Finally, the redox thermodynamics of B-class DyPs and the poor reactivity of Compound I are compared with data from other heme peroxidase (super)families as well as with chlorite dismutases (Clds). Clds share the conserved ferredoxin-like fold and have similar heme cavity architecture but exhibit completely different enzymatic activities.

2. Materials and methods

Cloning, site directed mutagenesis, expression and purification of *Kp*DyP and the variants D143A, R232A and D143A/R232A were described recently [4]. All chemicals were reagent grade.

2.1. Spectroelectrochemistry

The standard reduction potential, $E^{\circ\prime}$, of the Fe(III)/Fe(II) couple was determined using a homemade optical transparent thin layer electrochemical (OTTLE cell [8–11]. The three-electrode configuration consisted of a gold minigrid working electrode (Buckbee–Mears), a homemade Ag/AgCl/KClsat microreference electrode, separated from the working solution by a Vycor set, and a platinum wire as the counter electrode [8–11]. The reference electrode was calibrated against a saturated calomel (HgCl) electrode before each set of measurements. All potentials are referenced to the standard hydrogen electrode. Potentials were applied across the OTTLE cell with an Amel model 2053 potentiostat/galvanostat. A constant temperature was maintained by a circulating water bath and the OTTLE cell temperature was monitored with a copper-costan micro thermocouple. UV–vis spectra were recorded using a Varian Cary C50 spectrophotometer (Agilent Technologies, Santa Clara, CA, USA). The OTTLE cell was flushed with argon gas to establish an oxygen-free environment in the cell. Spectro-electrochemical titrations were performed using 650 µL samples containing 15 µM heme protein in 100 mM phosphate buffer, pH 7.0, and 100 mM NaCl, in presence of 25 µM methyl viologen and 1 µM lumiflavin 3-acetate, methylene blue, phenazine methosulfate, and indigo disulfonate, acting as redox mediators. Nernst plots consisted of at least five points and were invariably linear with a slope consistent with a one-electron reduction process.

Variable-temperature experiments were performed using a non-isothermal cell configuration [12]. The temperature of the reference electrode and the counter electrode was kept constant, whereas that of the working electrode was varied [12]. Parametrization of enthalpic and entropic components of $E^{\circ\prime}$ was possible via calculation of $\Delta S^{\circ\prime}_{rc}$ from the slope of the plot of $E^{\circ\prime}$ versus temperature; $\Delta H^{\circ\prime}_{rc}$ could be obtained from the Gibbs–Helmholtz equation, thus from the slope of the plot $E^{\circ\prime}/T$ versus $1/T$ [12]. Experiments with wild-type *Kp*DyP and variants were conducted over a temperature range from 15 to 40 °C.

2.2. Molecular dynamics simulations

Molecular dynamics simulations of wild-type *Kp*DyP (PDB entry 6FKS) and the variants D143A (6FL2), R232A (6FKT) and D143A/

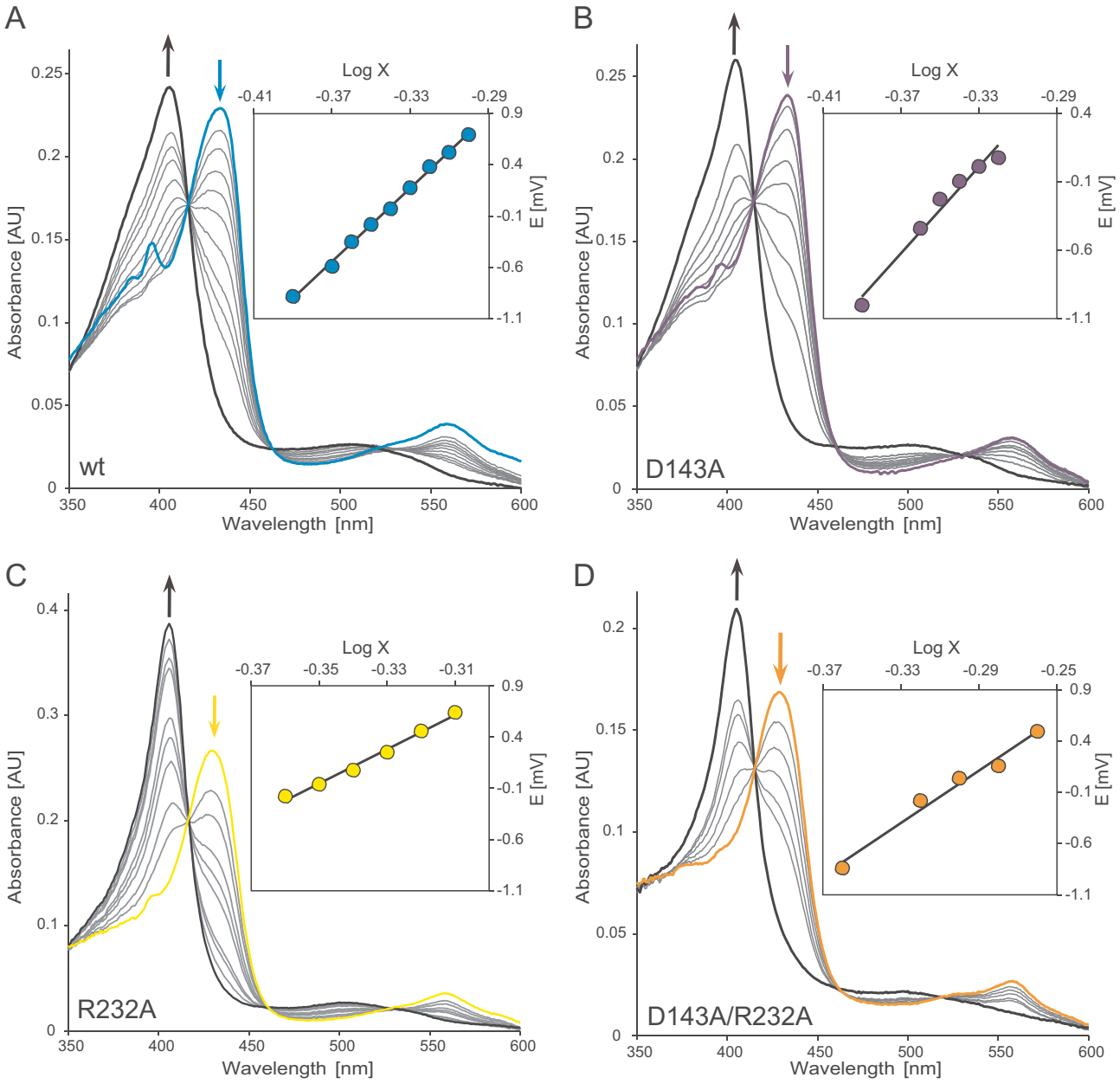

Fig. 2. Spectroelectrochemical titration of wild-type *Kp*DyP and the variants D143A, R232A and D143A/R232A. Shown are electronic absorption spectra of the four proteins at different applied potentials. The bold black spectra represent the fully oxidized state, whereas the bold colored spectra represent the fully reduced state of wild-type *Kp*DyP (A), D143A (B), R232A (C) and D143A/R232A (D), respectively at 25 °C (100 mM phosphate buffer, pH 7.0, and 100 mM NaCl). The insets depict the corresponding Nernst plots, where X represents $(A_{\lambda,redMax} - A_{\lambda,red}) / (A_{\lambda,oxMax} - A_{\lambda,ox})$.

R232A (6FIY) with a reduced and oxidized heme *b* were performed using the GROMOS11 molecular simulation package [13] and GROMOS force field 54A7 [14]. The reduced and the oxidized forms of the heme *b* were parametrized using the parameters previously published by Zou et al. and were linked to the coordinating histidine H215 [15]. Subsequently, the structures were relaxed by an in vacuo steepest descent energy minimization with a convergence criterion of 0.1 kJ/mol. The proteins were solvated in periodic rectangular simulation boxes containing the simple point charge water model [16] with a minimal solute-wall distance of 0.8 nm. Unfavorable solute-solvent contacts were removed by another energy minimization. Chloride and sodium counterions were added to create an overall neutral system at pH 7. The systems were gradually heated to 300 K with 60 K increases in temperature every 20 ps and equilibrated at a constant pressure for 100 ps.

Plain MD simulations were subsequently performed for 30 ns, using a step size of 2 fs. Coordinates were written out every 0.5 ps. Temperature and pressure were kept constant at 300 K and 1 atm, respectively. This was achieved through weak coupling with a relaxation time of 0.1 ps for the temperature and 0.5 ps for the pressure [17]. The isothermal compressibility was set to 4.575×10^{-4} $(kJ\,mol\,nm^{-3})^{-1}$. Bond lengths were constrained to their optimal values with a relative geometric accuracy of 10^{-4} using the SHAKE algorithm [18]. The nonbonded interactions were calculated using a twin-range cutoff [19], and a molecular pairlist, with a short-range cutoff of 8 nm and a long-range cutoff of 1.4 nm. A reaction-field contribution [20] was added to the electrostatic interactions and forces to account for a homogeneous medium outside the cutoff using a dielectric permittivity of 61 [21].

To analyze the amount and behavior of the water molecules in the binding pocket and substrate channels, the radial distribution function was calculated using the GROMOS++ package for the analysis of

biomolecular simulation trajectories [22]. The radial distribution function $g(r)$ is defined here as the probability of finding a particle of type j at distance r from a central particle i relative to the same probability for a homogeneous distribution of particles j around i. Program rdf calculates $g(r)$ for a number of discrete distances r, separated by distance dr as

$$g(r) = \frac{N_j(r)}{4\pi r^2 dr \rho_j}$$

where $N_j(r)$ is the number of particles of type j found at a distance between $r - 1/2\ dr$ and $r + 1/2\ dr$ and ρ_j is the number density of particles j. Integration of $N_j(r)$ gives the total number of water molecules N up to a maximum distance R.

$$N = \int_0^R N_j(r)dr = 4\pi\rho_j \int_0^R g(r)r^2 dr$$

CAVER 3.0 [23] was used to detect tunnels and analyze the dynamics of putative substrate channels of wild-type *Kp*DyP and the variants (PDB entries see above). For channel calculation the heme iron was set as the starting point, water and ion molecules were excluded. Snapshots from MD simulations were taken every 500 ps (total 61 frames). Shell radius was set to 4, shell depth to 10 and probe radius to 0.9. The clustering threshold was set to 4.5, resolution for tunnel bottleneck radius was set to 0.25 nm.

3. Results

Wild-type homodimeric *Kp*DyP and variants were expressed heterologously in *E. coli* and purified by affinity and size-exclusion chromatography as described recently [4]. Typically, 60–80 mg wild-type and variant heme protein per liter culture broth were obtained. The average Reinheitszahl (RZ, ASoret/A280) was found to be 2.1 (wild-type *Kp*DyP), 1.7 (D143A) and 2.7 (R232A and D143A/R232A), respectively. The UV–vis and EPR spectral signatures of wild-type *Kp*DyP and the variants indicated that all iron proteins are in the high-spin (HS) state at pH 7.0 [4]. Wild-type *Kp*DyP exhibits UV–vis bands at 405 nm (Soret band) together with a small shoulder at 385 nm, 510 nm and 539 nm (Q-bands) and 640 nm [charge transfer (CT) band]. Except for the broad Soret maximum around 400 nm the spectrum of ferric D143A variant is identical with that of the wild-type protein. In the variants R232A and D143A/R232A the CT band is blue-shifted, whereas the other bands are almost wild-type-like (Fig. S1) [4]. Importantly, the recombinantly produced variants D143A, R232A and D143A/R232A show wild-type-like ECD-spectra in the far- and near-UV region (not shown). Moreover, the available high resolution crystal structures of wild-type *Kp*DyP and the investigated variants [4] clearly show that all four proteins are correctly folded.

First, we probed the standard reduction potential ($E^{\circ\prime}$) of the Fe(III)/Fe(II) redox couple of wild-type *Kp*DyP and the variants D143A, R232A and D143A/R232A at pH 7.0 by spectro-electrochemistry (Fig. 2, Table 1). Upon reduction of ferric to ferrous wild-type *Kp*DyP the Soret peak shifts from 405 nm to 435 nm. Fig. 2A shows the fully oxidized (bold black line) and fully reduced (bold blue line) and equilibrium spectra of wild-type *Kp*DyP (black lines) at different applied potentials

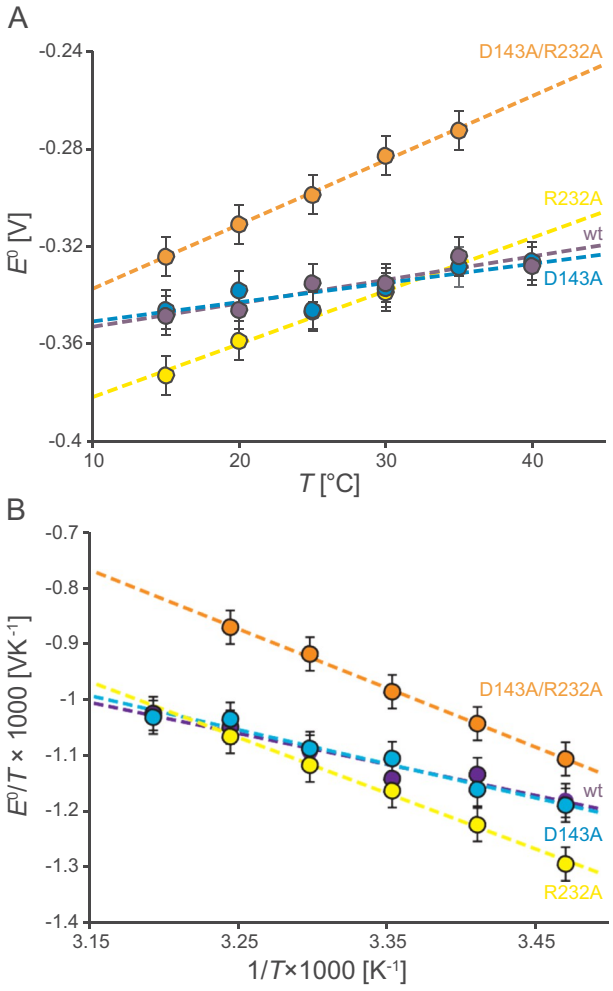

Fig. 3. Redox thermodynamics of the high-spin native form of *Kp*DyP and the variants D143A, R232A, and D143A/R232A. (A) Temperature dependence of the reduction potential $E^{\circ\prime}$
(B) Plot of $E^{\circ\prime}/T$ versus $1/T$. *Kp*DyP (violet), D143A (blue), R232A (yellow) and D143A/R232A (orange). The slopes of the plots yield the $\Delta S^{\circ\prime}_{rc}/F$ (A) and $-\Delta H^{\circ\prime}_{rc}/F$ (B), respectively. Solid lines are least-squares fits to the data points. All experiments were conducted in 150 mM phosphate buffer and 100 mM NaCl at pH 7.0. (For interpretation of the references to color in this figure legend, the reader is referred to the web version of this article.)

Table 1
Thermodynamic parameters for the Fe(III) → Fe(II) reduction of high-spin native class B dye-decolorizing peroxidase from *Klebsiella pneumoniae* (*Kp*DyP) and the variants D143A, R232A and D143A/R232A. For comparison, the thermodynamic parameters of the structurally related chlorite dismutase from "Nitrospira defluvii" (NdCld) [37] and *N. winogradskyi* (NwCld) [37] and of heme peroxidases from different peroxidase superfamilies [2] are shown. HRP, horseradish peroxidase [12]; KatG, catalase-peroxidase from *Synechocystis* PCC 6803 [36]; MPO, myeloperoxidase [10]; wt, wild-type.

Protein	E° (V)	$\Delta H^{\circ\prime}_{rc}$ (kJ/mol)	$\Delta S^{\circ\prime}_{rc}$ (J/mol∗K)	$-\Delta H^{\circ\prime}_{rc}/F$ (V)	$T\Delta S^{\circ\prime}_{rc}/F$ (V)	$\Delta H^{\circ\prime}_{rc(int)}$ ($=\Delta G^{\circ\prime} = -nFE^{\circ\prime}$) (kJ/mol)
wt *Kp*DyP	−0.350	54	76	−0.560	0.235	34
D143A	−0.330	59	93	−0.611	0.287	32
R232A	−0.347	97	210	−1.005	0.649	33
D143A/R232A	−0.299	104	254	−1.078	0.785	29
*Nd*Cld	−0.113	29	63	−0.305	0.194	11
*Nw*Cld	−0.119	40	95	−0.413	0.292	11
HRP	−0.306	91	210	−0.943	0.649	30
KatG	−0.226	17	−18	−0.176	−0.056	22
MPO	0.005	3	10	−0.031	0.031	0

in the optical transparent thin-layer spectroelectrochemical (OTTLE) cell (25 °C, pH 7.0). The calculated reduction potential $E^{\circ\prime}$ for the Fe(III)/Fe(II) couple, determined from the corresponding Nernst plot (inset to Fig. 2A), was calculated to be −0.350 ± 0.0010 V (Table 1). Exchange of D143 slightly increases the standard reduction potential (D143A: −0.330 ± 0.010 V, Table 1) compared to the wild-type protein (Fig. 2B), whereas $E^{\circ\prime}$ is almost unaffected by mutation of R232 (R232A: −0.347 ± 0.010 V) (Fig. 2C, Table 1). The $E^{\circ\prime}$ value of D143A/R232A was calculated to be −0.299 ± 0.010 V (Fig. 2D, Table 1).

To gain deeper insight into the mechanism of $E^{\circ\prime}$ modulation in B-class DyPs, the temperature dependence of the reduction potential of the high-spin forms was investigated (Fig. 3). This allows parametrization of the enthalpic ($\Delta H^{\circ\prime}_{rc}$) and entropic ($\Delta S^{\circ\prime}_{rc}$) components of the Fe(III) to Fe(II) reduction reaction. For wild-type *Kp*DyP and variants the oxidized state is enthalpically stabilized over the reduced state with D143A/R232A (104 kJ/mol) > R232A (97 kJ/mol) > D143A (59 kJ/mol) > wild-type *Kp*DyP (54 kJ/mol) (Table 1). Reduction of all proteins is entropically favored, with D143A/R232A (254 J/mol·K) > R232A (210 J/mol·K) > D143A (93 J/mol·K) > wild-type *Kp*DyP (76 J/mol·K) (Table 1). The resulting entropic contributions to $E^{\circ\prime}$ partially compensate for the enthalpic stabilization of the ferric state (see comparison of $-\Delta H^{\circ\prime}_{rc}/F$ and $T\Delta S^{\circ\prime}_{rc}/F$ in Table 1). The obtained data clearly demonstrate that (i) the negative $E^{\circ\prime}$ values of the four proteins is due to the large enthalpic term, which outweighs the entropic contribution, and that (ii) exchange of R232 but not of D143 significantly alters the reduction thermodynamics.

Next, molecular dynamics simulations were performed to evaluate differences in protein structure and solvation between the ferric and ferrous state of the four proteins. Based on the respective crystal structures [4], the proteins were simulated for 30 ns in their oxidized and reduced heme states. It has to be mentioned that the structures as deposited in the PDB are in the reduced state due to X-ray radiation-derived electrons [24]. The backbone atom-positional root-mean-square deviations (rmsd) between the respective crystal structure and the ferric or ferrous state after a 30 ns simulation were 1.9 and 2.5 Å (wild-type *Kp*DyP), 1.7 and 2.0 Å (D143A), 2.5 and 2.2 Å (R232A), and 2.5 and 1.9 Å (D143A/R232A), respectively, demonstrating that the overall protein structures in both redox states are highly similar. Additionally, no changes in the structure and planarity of the heme group were observed. These findings suggest that reduction of ferric wild-type *Kp*DyP and the variants to the ferrous state alters neither the overall nor the active site structures of the respective proteins.

In order to evaluate differences in solvation between the ferric and ferrous state of the four proteins at the active site, we solved the radial distribution function (rdf) for water in the heme cavity, which is defined as the probability of finding a H_2O molecule at a given distance from the heme iron relative to the same probability for a homogeneous distribution of water. Fig. 4 depicts the number of water molecules calculated from the radial distribution function in the ferric (red lines) and ferrous (black line) states of the wild-type protein and the three variants up to a distance of 10 Å (i.e. the point at which the bulk solvent is reached). In the reduced state the water dipoles are located further away from the metal ion compared to the Fe(III) state (see spikes in Fig. 4) reflecting solvent reorganization during the Fe(III) to Fe(II) reduction reaction. The lower solvent organization in the Fe(II) state is further indicated by the comparably more diffuse shape of the rdf (i.e. less defined spikes, compared to the Fe(III) species).

To investigate this further, the accumulated number of water molecules at a given distance was calculated from integration of the radial distribution of the number of water molecules, $N_j(r)$. As can be seen in Fig. 4 (gray area) the first hydration sphere (2 Å) in the Fe(III) state is always occupied by a water molecule, while it remains empty in the Fe(II) state. The occurrence of water in the Fe(II) state in the second hydration shell (~5 Å distance) is also significantly lower and less ordered than in the Fe(III) state, with a single accumulated water molecule at 5 Å distance in the Fe(II) compared to three in the Fe(III) state.

Fig. S2 depicts the difference in number of water molecules, Δn_{H_2O}, in the oxidized and reduced state. In all four ferric proteins a water molecule acts as distal ligand of the heme iron. Between 5 Å and 8 Å from the heme iron the variants D143A and D143A/R232A in the ferric state accommodate significantly more water molecules compared to the Fe(II) state [Δn_{H_2O}, = 4 in D143A and 2 in D143A/R232A] (Fig. S2). By comparison in the same interval, the number of water molecules in ferric wild-type *Kp*DyP is much lower compared to the reduced state.

Next we probed the impact of mutations on the access routes of H_2O (and H_2O_2) molecules to the heme *b* cofactor and the dynamics of those channels. In wild-type *Kp*DyP there are two main access routes to the active site. One is suggested to be the main access channel (i.e. channel 1) for H_2O_2 leading from the protein surface almost perpendicularly to the heme plane above the metal ion (length: 14.7 Å) [4]. The main bottleneck is formed by four amino acids, namely the highly conserved catalytic amino acids D143 and R232 as well as the equally well conserved L246 and F248 (bottleneck radius: 1.6 Å). The second access channel (i.e. channel 2) is via a surface exposed propionate group, which is lined by highly flexible lysine residues (length 16.7 Å; bottleneck radius: 1.5 Å). The crystal structures of the variants D143A, R232A and D143A/R232A demonstrate that both access routes are influenced by the introduced mutations [4].

Using CAVER 3.0 [23] two additional access routes (i.e. channels 3 & 4) have been calculated besides the two main access channels described above (Table 2). We have analyzed the clustering of these four potential channels over the course of the MD simulations (i.e. 30 ns) for both the ferric and ferrous state (Fig. 5 and Table 2). For ferric wild-type *Kp*DyP and D143A channel 1 shows the highest occurrence (Fig. 5, red cluster) allowing the passage of H_2O and H_2O_2. It was found in all analyzed snapshots of D143A and 89% of snapshots of the wild-type protein. In addition channel 2 (Fig. 5, dark blue cluster) provides access to the heme iron in wild-type *Kp*DyP but not in D143A (bottleneck radius ~ 1.2 Å). Channels 3 and 4 (Fig. 5, yellow and cyan clusters) are negligible. In ferric R232A and D143A/R232A both channel 1 and 2 may act as access routes with R232A showing the lowest occurrence (61%) of channel 1 of the four studied proteins. Additionally, channel 3 (but not channel 4) seems to provide an alternative substrate channel for both variants.

Table 2 compares the channel characteristics of the four proteins in the ferric and ferrous states. Except for wild-type *Kp*DyP, where it occurs less frequently in the ferrous state, channel 1 exhibits similar occurrence and channel properties in the variants in both oxidation states. In ferrous D143A/R232A both channel 1 and 2 seem to provide access with similar occurrence and channel characteristics. In ferrous wild-type *Kp*DyP and D143A the channels 2, 3 and 4 are unlikely to provide access to the active site, whereas in R232A all four channels would allow for access of water.

Next we analyzed the occurrence and bottleneck characteristics of channel 1 over the course of the MD simulation in all four proteins in detail (Fig. S3 provides the corresponding data for channels 2, 3 and 4). Fig. 6 depicts the molecular dynamics of the channel characteristics over the 30 ns simulation period with bottleneck radii represented by color (magenta = smaller radius, green = wider radius) over the length of the tunnel (i.e. 16 Å). Wild-type *Kp*DyP and the variant R232A exhibit the most restricted accessibility (lowest bottleneck radius and lowest occurrence). The wild-type protein shows some shifts in location of the bottleneck radius away from the area immediately above the heme iron during simulation, likely due to movement of D143. The variant D143A shows a high accessibility with no significant change over the course of the simulation. By contrast, channel 1 shows low occurrence in R232A (many time frames with no detectable channel) with the bottleneck being between 5 and 10 Å away from the heme iron during simulation. The double-variant appears to be significantly more open than R232A.

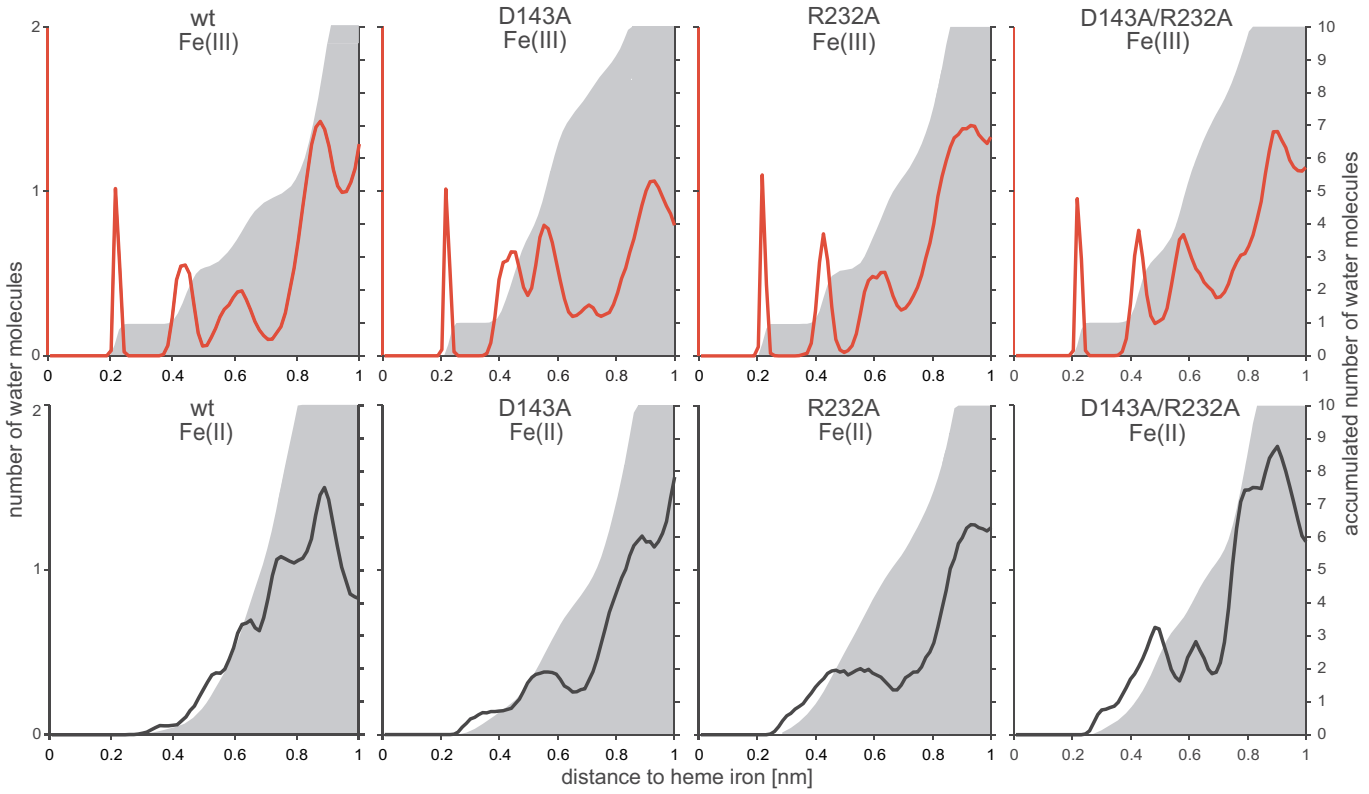

Fig. 4. Number of water molecules calculated from the radial distribution function in high-spin ferric and ferrous wild-type *Kp*DyP and the variants D143A, R232A, and D143A/R232A. Radial distribution function with respect to the heme iron of the oxidized states (red, top panel) and the reduced states (bottom panel, black). The number of accumulated water molecules in a distance of up to 1 nm (corresponding to the distance between bulk water and heme *b* cofactor) is shown in gray. (For interpretation of the references to color in this figure legend, the reader is referred to the web version of this article.)

In ferrous wild-type *Kp*DyP and R232A the channel characteristics are similar to those of the ferric state. The variants D143A and D143A/R232A show significantly lower bottleneck radii close to the heme (up to 5 Å) in the ferrous form.

4. Discussion

Despite sharing a well conserved two-domain structure and α + β ferredoxin-like fold and active site residues the three phylogenetic classes of dye-decolorizing peroxidases show a broad functional diversity [3]. Whereas A- and C/D-class DyPs seem to acts as peroxidases and efficiently catalyze the hydrogen peroxide-mediated one-electron oxidation of substrates (AH) of diverse molecular structures (H_2O_2 + 2 AH → 2 A· + 2 H_2O), B-class DyPs are very poor peroxidases. Therefore various alternative enzymatic functions have been suggested for this class [5–7]. Typically, a peroxidase cycle includes formation of Compound I [oxoiron(IV) porphyryl radical] by H_2O_2-mediated oxidation of the ferric heme peroxidase according to reaction (1) followed by one-electron reduction of Compound I to Compound II [oxoiron(IV)] (reaction (2)) and, finally, reduction of Compound II back to the ferric resting state [Fe(III) Por] (reaction (3)).

$$[\mathrm{Fe(III)\ Por}] + H_2O_2 \rightarrow [\mathrm{Fe(IV) = O\ Por^{\bullet+}}] + H_2O \quad (1)$$

$$[\mathrm{Fe(IV) = O\ Por^{\bullet+}}] + \mathrm{AH} \rightarrow [\mathrm{Fe(IV) - OH}] + \mathrm{A^{\bullet}} \quad (2)$$

$$[\mathrm{Fe(IV) - OH}] + \mathrm{AH} \rightarrow [\mathrm{Fe(III)\ Por}] + H_2O + \mathrm{A^{\bullet}} \quad (3)$$

Recently, we demonstrated that reaction (1) in B-class DyP from *Klebsiella pneumoniae* (*Kp*DyP) is fast ($6.2 \times 10^6\ M^{-1}\ s^{-1}$), monophasic, and pH-independent between pH 4 and pH 9 [4]. Additionally, both electron paramagnetic resonance and UV–vis spectroscopic data revealed the electronic structure of Compound I to be an oxoiron(IV) porphyrin radical species. Furthermore, our data suggested that D143 acts as acid-base catalysts in Compound I formation with the p*K*a of D143 being far below 4.0 due to stabilization of the conjugated base by the proximity to the R232 guanidinium group. In the absence of D143 the apparent bimolecular rate constant of Compound I formation is reduced by 3 orders of magnitude [4]. Most interestingly, Compound I of wild-type *Kp*DyP is very stable, as is reflected by the absence of spectral shifts over a long time period (> 10 min). No spectral shift to a Compound I* was observed [i.e. oxoiron(IV) protein radical] demonstrating absence of internal electron transfer [4].

At physiological pH B-class DyPs exist in the high-spin ferric state with a water molecule coordinating the heme iron at the distal site. Heme *b* is coordinated by a proximal histidine (H215), which is hydrogen-bonded with a fully conserved aspartate (D268). The negative $E^{\circ\prime}$ of the Fe(III)/Fe(II) couple of −350 mV clearly suggests a pronounced imidazolate character of H215 in *Kp*DyP, similar to heme peroxidases from the peroxidase-catalase and peroxidase-cyclooxygenase superfamilies [8–10,12].Other B-class DyPs, feature more positive $E^{\circ\prime}$ values (e.g. −260 mV in DyP from *Pseudomonas putida* [25] and −290 mV in DyP from *Enterobacter lignolyticus* [26]).

The relative contributions of $\Delta H^{\circ\prime}_{rc}$ and $\Delta S^{\circ\prime}_{rc}$ to the reduction reaction (Table 1) demonstrated that the ferric state in native B-class is enthalpically stabilized (54 kJ/mol), whereas formation of the ferrous state is entropically favored (76 J/mol*K). Reduction enthalpy and entropy contain contributions from both intrinsic protein-based factors ($\Delta H^{\circ\prime}_{rc,int}$ and $\Delta S^{\circ\prime}_{rc,int}$) and solvent-based factors ($\Delta H^{\circ\prime}_{rc,solv}$ and $\Delta S^{\circ\prime}_{rc,solv}$):

$$\Delta H^{\circ\prime}_{rc} = \Delta H^{\circ\prime}_{rc,int} + \Delta H^{\circ\prime}_{rc,solv} \text{ and } \Delta S^{\circ\prime}_{rc} = \Delta S^{\circ\prime}_{rc,int} + \Delta S^{\circ\prime}_{rc,solv}.$$

Our MD simulations have shown that the structure of wild-type *Kp*DyP (and the proteins) in the Fe(III) and Fe(II) forms are very similar ($\Delta S^{\circ\prime}_{rc,int} \approx 0$), suggesting that reduction entropy mainly reflects solvent reorganization effects ($\Delta S^{\circ\prime}_{rc} \approx \Delta S^{\circ\prime}_{rc,solv}$). This agrees with

Table 2
Channel cluster characteristics of wild-type ferric and ferrous class B dye-decolorizing peroxidase from *Klebsiella pneumoniae* (*Kp*DyP) and the variants D143A, R232A and D143A/R232A. wt, wild-type; DM, double variant (D143A/R232A).

Channel	Variant	# snaps	Occurrence %	Priority	Bottleneck radius	Throughput	Length
Fe(III)							
1	wt	54	89	0.5	1.6	0.57 ± 0.07	14.7 ± 2.7
	D143A	61	100	0.7	1.6	0.71 ± 0.06	14.6 ± 1.5
	R232A	37	61	0.3	1.5	0.55 ± 0.09	14.6 ± 2.5
	DM	61	100	0.7	1.6	0.71 ± 0.05	14.6 ± 2.9
2	wt	41	67	0.4	1.5	0.53 ± 0.08	16.7 ± 2.3
	D143A	53	87	0.3	1.2	0.39 ± 0.07	19.6 ± 2.5
	R232A	50	82	0.3	1.5	0.40 ± 0.07	22.1 ± 3.2
	DM	44	72	0.4	1.6	0.54 ± 0.09	19.3 ± 4.8
3	wt	36	59	0.2	1.1	0.32 ± 0.06	22.3 ± 3.4
	D143A	27	44	0.2	1.2	0.44 ± 0.08	17.7 ± 3.1
	R232A	25	41	0.3	1.5	0.62 ± 0.07	10.4 ± 2.0
	DM	46	75	0.4	1.5	0.50 ± 0.07	17.5 ± 2.4
4	wt	21	34	0.1	1.2	0.38 ± 0.10	23.0 ± 5.9
	D143A	18	30	0.1	1.1	0.26 ± 0.09	28.7 ± 5.5
	R232A	13	21	0.1	1.1	0.36 ± 0.05	20.1 ± 2.1
	DM	39	64	0.2	1.1	0.31 ± 0.06	24.9 ± 3.4
Fe(II)							
1	wt	44	73	0.4	1.6	0.53 ± 0.1	18.7 ± 4
	D143A	59	98	0.6	1.6	0.59 ± 0.05	16.6 ± 2.5
	R232A	38	63	0.3	1.5	0.55 ± 0.07	14.9 ± 2.1
	DM	60	100	0.6	1.6	0.61 ± 0.06	17.6 ± 1.46
2	wt	38	63	0.2	1.2	0.33 ± 0.08	25.8 ± 3.2
	D143A	31	52	0.2	1.1	0.31 ± 0.05	24.3 ± 3.5
	R232A	37	62	0.3	1.5	0.43 ± 0.07	22.3 ± 2.6
	DM	58	97	0.5	1.5	0.55 ± 0.09	16.3 ± 3.3
3	wt	28	47	0.2	1.4	0.38 ± 0.089	21.6 ± 3.2
	D143A	20	33	0.1	1.2	0.41 ± 0.03	25.8 ± 2
	R232A	24	40	0.2	1.5	0.57 ± 0.074	12.8 ± 2.2
	DM	30	50	0.2	1.6	0.47 ± 0.12	21.9 ± 2.4
4	wt	11	18	0.1	1.0	0.26 ± 0.05	29.8 ± 4.4
	D143A	21	35	0.1	1.1	0.27 ± 0.04	27 ± 2.5
	R232A	18	30	0.1	1.4	0.34 ± 0.06	26.2 ± 2.5
	DM	23	38	0.1	1.1	0.38 ± 0.08	21.1 ± 3.1

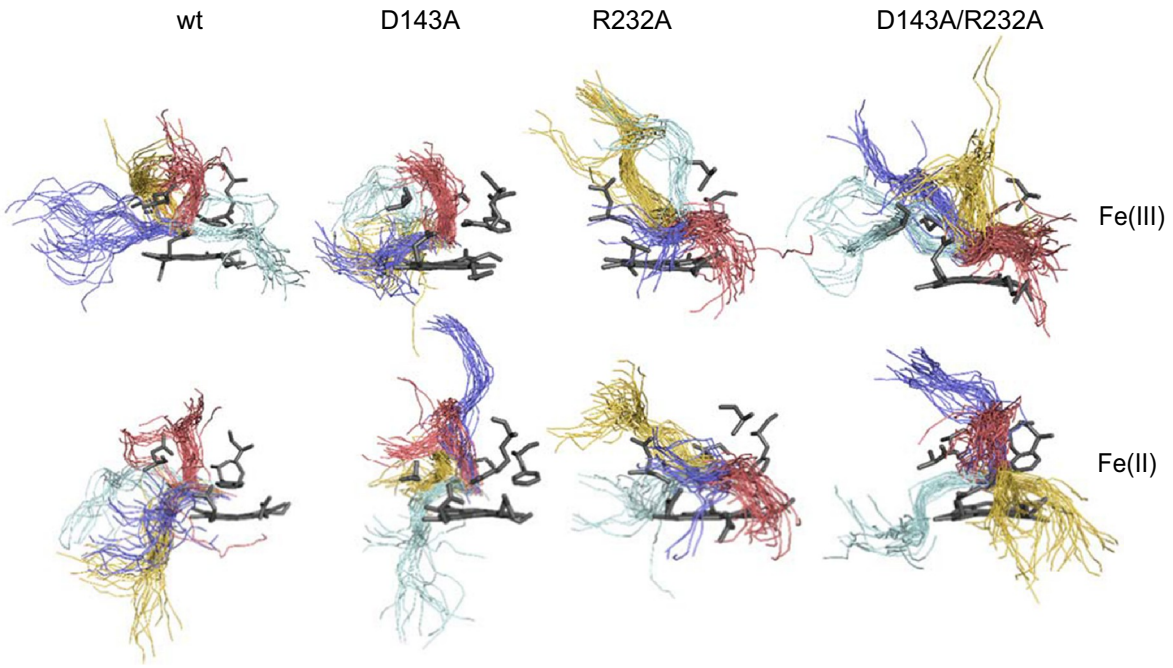

Fig. 5. Clustering of the four top ranked access channels in high-spin ferric and ferrous wild-type *Kp*DyP and the variants D143A, R232A, and D143A/R232A. Clustering of channel 1 (red), 2 (dark blue), 3 (yellow) and 4 (cyan) was analyzed throughout the molecular dynamics simulation of the four proteins using CAVER 3.0 [22]. The clusters are presented in one frame (MD structure after 30 ns simulation) as pathway centerlines. The heme *b* cofactor and the amino acid residues lining the channel bottleneck in wild-type *Kp*DyP are shown as sticks (dark gray). (For interpretation of the references to color in this figure legend, the reader is referred to the web version of this article.)

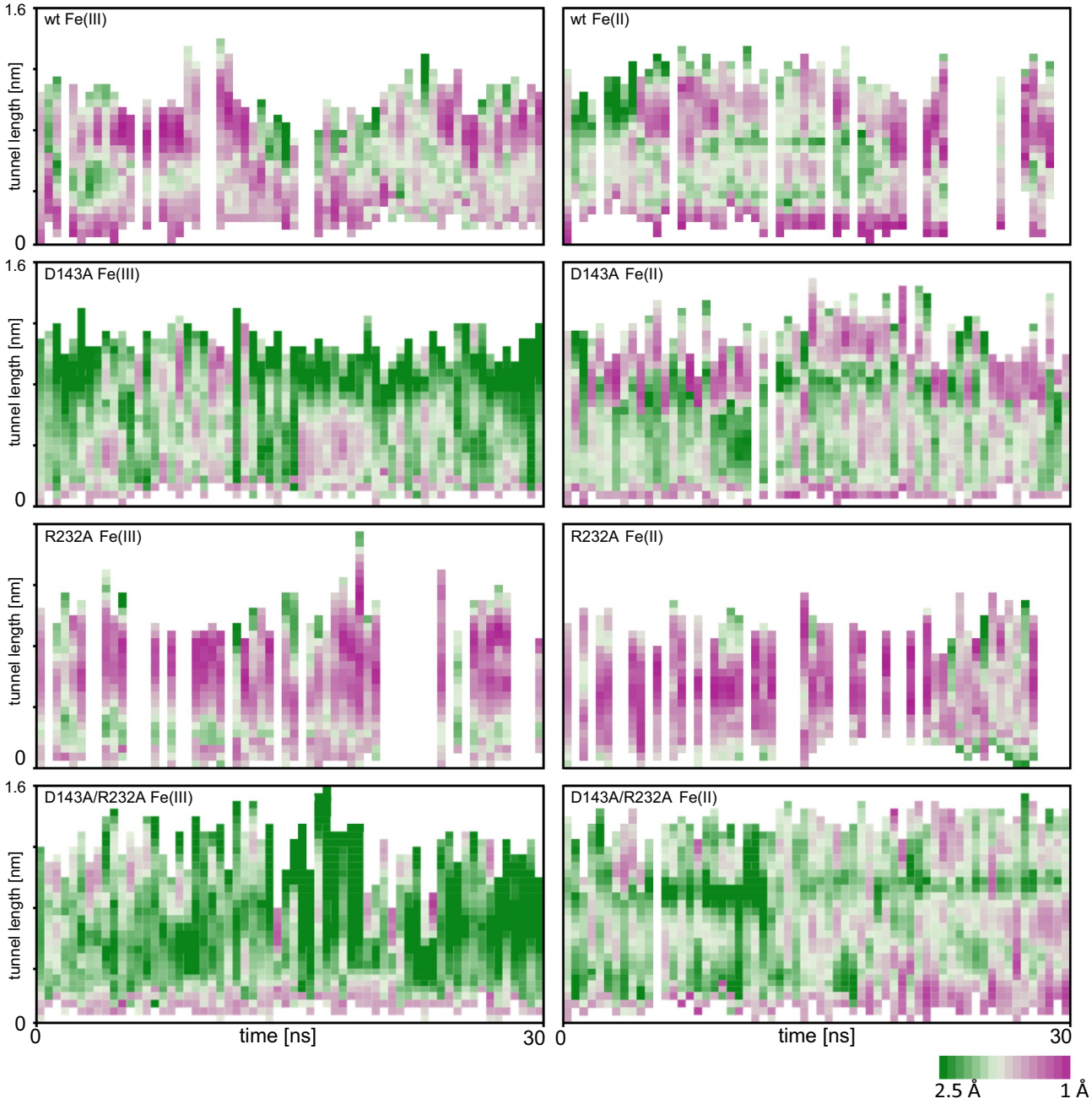

Fig. 6. Dynamics of characteristics of the main access route in high-spin ferric and ferrous wild-type *Kp*DyP and the variants D143A, R232A, and D143A/R232A. Variations of tunnel lengths and radii during 30 ns MD simulation are shown. The color map ranges from very narrow (magenta) to wide (green) bottleneck. White lines show that in the given snapshot no tunnel with a bottleneck radius ≥ 0.9 Å was found. (For interpretation of the references to color in this figure legend, the reader is referred to the web version of this article.)

available data for the ferric and ferrous forms of other heme proteins which indicate that, in general, reduction-induced structural changes are quite small [8–12].

Because reduction-induced solvent reorganization effects usually induce compensatory enthalpic and entropic changes (i.e. $\Delta H^{\circ\prime}_{rc,solv} = T\cdot\Delta S^{\circ\prime}_{rc,solv}$), the protein-based contribution to

$$\Delta G^{\circ\prime}rc = -nFE^{\circ\prime} = \Delta H^{\circ\prime}_{rc} - T\cdot\Delta S^{\circ\prime}_{rc}$$
$$= \Delta H^{\circ\prime}_{rc,int} + \Delta H^{\circ\prime}_{rc,solv} - T\cdot\Delta S^{\circ\prime}_{rc,solv}$$

can be estimated [11,27,28]:

$$\Delta G^{\circ\prime}rc = -nFE^{\circ\prime} \approx \Delta H^{\circ\prime}_{rc,int}.$$

Hence, to a first approximation the measured $E^{\circ\prime}$ values coincide with $\Delta H^{\circ\prime}_{rc,int}$. In *Kp*DyP they are determined by the significant enthalpic stabilization of the ferric state ($\Delta H^{\circ\prime}_{rc,int}/F = -560$ mV) due to the interaction of the heme iron with the (anionic) imidazolate of H215 and the polarity of the distal cavity, which electrostatically stabilizes the positively charged Fe(III) state over the electrostatically uncharged Fe(II) state. The distal heme cavity of DyPs are characterized by a complex H-bonding network involving D143, R232, four water molecules and heme propionate at position 6.

The positive reaction entropy values of wild-type *Kp*DyP can be attributed to a decrease in solvent ordering upon reduction ($\Delta S^{\circ\prime}_{rc} \approx \Delta S^{\circ\prime}_{rc,solv}$), due to dissociation of the axial water following heme Fe(III) reduction and to reduced electrostatic interaction of water with Fe(II). Exact enthalpy-entropy compensation for solvent degrees of

freedom, as is observed in wild-type *Kp*DyP, is known to occur in many processes and therefore $\Delta H^{\circ\prime}_{rc,solv} = T \cdot \Delta S^{\circ\prime}_{rc,solv}$ is experimentally supported [29–31]. This is further confirmed by the MD simulation derived rdf, which clearly shows the differences in solvent occurrence and ordering between the ferric and ferrous forms of wild-type *Kp*DyP. A higher water ordering implies a significantly more stable hydrogen bonding network in the ferric state.

With respect to proximal heme ligation, polarity of the distal heme cavity and redox thermodynamics B-class DyPs are similar to heme peroxidases from other superfamilies (Table 1) [2,8]. The $E^{\circ\prime}$[Fe(III)/Fe(II)] of −350 mV is very negative but falls in the range reported for heme *b* peroxidases (i.e. with unmodified prosthetic group) [8]. More positive $E^{\circ\prime}$ values are found in the members of peroxidase-cyclooxygenase superfamily (which share a proximal imidazolate ligand and a polar distal cavity), because the prosthetic group is posttranslationally modified, i.e. it is bound to the protein via up to three covalent links (Table 1) [2,32–35]. Chlorite dismutases (Clds) (which have a similar overall fold and heme cavity architecture) feature $E^{\circ\prime}$[Fe(III)/Fe(II)] values significantly more positive (−113 mV and −119 mV) [37]. This is due to (i) the lower imidazolate character of the proximal histidine and (ii) the apolar distal heme cavity containing only one charged amino acid residue, i.e. a mobile catalytic arginine [38].

In order to oxidize ferric B-class DyP to Compound I according to reaction (1) hydrogen peroxide must have access to the heme cavity. The crystal structure of *Kp*DyP [4] and the MD simulations of this work clearly revealed two access channels. The main access route (channel 1) leads perpendicularly from the protein surface to the heme cavity with a bottleneck formed by the distal amino acids D143, R232, L246 and F248 in close proximity to the heme (radius of 1.6 Å). The second access route (channel 2) is relatively open at the protein surface (solvent-exposed propionate at position 6) and steadily narrows leading to a bottleneck with a radius of 1.5 Å that also restricts direct access to the heme iron. Hydrogen peroxide likely enters the heme cavity via channel 1 and is deprotonated at D143. The resulting anion binds to Fe(III) (i.e. formation of Compound 0) and rapidly mediates the two-electron oxidation of the enzyme to Compound I (reaction (1)). The rate of Compound I formation in *Kp*DyP is similar to heme peroxidases from other superfamilies that use a distal histidine as base for H_2O_2 deprotonation [2,4].

Exchange of D143 by alanine significantly decreases the rate of Compound I formation but keeps the heme cavity architecture wild-type-like [4]. The reduction thermodynamics are also only slightly affected by this mutation (Table 1). The lower $\Delta H^{\circ\prime}_{rc,int}$ of D143A compared to the wild-type protein (which is responsible for to the more positive $E^{\circ\prime}$ value) fits with the selective electrostatic stabilization of the ferrous form due to deletion of a negatively charged residue close to the heme. Exchange of D143 significantly increases solvent (and substrate) accessibility via channel 1 as is obvious from the comparison of MD simulations of channel 1 of wild-type *Kp*DyP and D143A (Fig. 6) as well as by calculation of the respective radial distribution function for water (Fig. S2). Most importantly, the reactivity of D143A towards conventional peroxidase substrates (reactions (2) & (3)) is several orders of magnitude higher compared to wild-type *Kp*DyP [4]. Since access via channel 2 is restricted in D143A (Table 2), the increased peroxidase activity must stem from increased access via channel 1.

It is reasonable to assume that the oxidation capacity of Compound I of wild-type *Kp*DyP and D143A is similar since, typically, $E^{\circ\prime}$ values of the Fe(III)/Fe(II) values strictly correlate with $E^{\circ\prime}$ values of the catalytically relevant redox couples Compound I/Compound II as well as Compound I/ferric state in heme peroxidases [8–10,32–34]. The more positive the $E^{\circ\prime}$ value of the redox couple Fe(III)/Fe(II) is (ranging from −350 to +50 mV) [8], the more unstable and reactive is Compound I of the respective peroxidase. As a consequence Compound I of wild-type *Kp*DyP and D143A is a poor oxidant compared to that of myeloperoxidase [10], which exhibits the most positive $E^{\circ\prime}$ value of the redox couple Fe(III)/Fe(II) (i.e. +50 mV) reported so far [8]. Thus the observed differences in kinetics of substrate oxidation between wild-type *Kp*DyP and D143A are solely caused by substrate accessibility and not redox thermodynamics.

Both D143 and R232 are fully conserved in DyPs. Besides the proposed role in electrostatic promotion of heterolysis of the O—O bond of hydrogen peroxide during Compound I formation [4], R232 is important for stabilization of the distal heme cavity by forming a salt bridge with the propionate at position 7. The crystal structure of variant R232A shows significant changes in the active-site conformation. Residues 142–148 were found in a completely different orientation compared with the wild-type structure, which forces the side-chain of D143 to point away from the heme [4]. Despite showing a wild-type-like $E^{\circ\prime}$ value of the Fe(III)/Fe(II) redox couple, the reduction thermodynamics of R232A - but also that of the double variant D143A/R232A - are significantly altered (Table 1). The high electrostatic stabilization of the ferric state, due to removal of the positively charged guanidinium group of R232, is nearly offset by the structural effects caused by reorganization of the loop formed by amino acids 142–148, which moves the sidechain of D143 away from the heme. Hence, it appears that the mutation does not have a big impact on the intrinsic contribution of the protein, but significantly influences the reduction-induced solvent reorganization. The lower $\Delta H^{\circ\prime}_{rc,int}$ of D143A/R232A compared to the wild-type protein and the single variants demonstrate that the impact exerted by the two mutations on $E^{\circ\prime}$ is not additive, with the effect of mutation of D143 exceeding that of exchange of R232. In both R232A and D143A/R232A access to the heme cavity is also possible via channel 3 in addition to channels 1 and 2. However, the double variant features significantly increased solvent accessibility compared to R232A (Figs. 6 and S2).

In summary, B-class DyP from *Klebsiella pneumonia* in its ferric resting state efficiently reacts with hydrogen peroxide, thereby forming a stable unreactive Compound I and water. The Fe(III) state is enthalpically stabilized, whereas the reduction reaction is entropically favored due to solvent reorganization upon reduction. The negative $E^{\circ\prime}$ value of the Fe(III)/Fe(II) couple suggests that the oxidation capacity of Compound I is smaller compared to heme peroxidases from other (super)families. The poor reactivity of wild-type *Kp*DyP Compound I is caused by the restricted access to the heme cavity. This is underlined by the fact that mutation of distal D143, which is essential as proton acceptor during heterolytic cleavage of H_2O_2, has almost no impact on the heme cavity architecture and redox thermodynamics. Nevertheless, the substrate access channel in D143A is increased and thus allows oxidation of typical peroxidase substrates. Exchange of R232 leads to a collapse of the distal heme cavity and alters the redox thermodynamics and access channels. The question about the physiological electron donor of *Kp*DyP Compound I remains open.

Abbreviations

DyP	dye-decolorizing peroxidase
*Kp*DyP	dye-decolorizing peroxidase from *Klebsiella pneumoniae*
$E^{\circ\prime}$	standard reduction potential
$\Delta H^{\circ\prime}_{rc}$	enthalpy change for the reaction center upon reduction of the oxidized protein
$\Delta S^{\circ\prime}_{rc}$	entropy change for the reaction center upon reduction of the oxidized protein
SHE	standard hydrogen electrode
rdf	radial distribution function; rmsd, root-mean-square deviation
OTTLE cell	optical transparent thin layer electrochemical cell
MD	molecular dynamics

Acknowledgments

This project was supported by the Austrian Science Fund, FWF [Doctoral program BioToP – Molecular Technology of Proteins

(W1224)] and the FWF projects I2429 and P30979.

Appendix A. Supplementary data

Supplementary information contains data about (i) spectral transition of fully oxidized native high-spin wild-type *Kp*DyP and the variants D143A, R232A, and D143A/R232A to the ferrous state mediated by dithionite (Fig. S1), (i) the difference in the number of water molecules at increasing distance from the heme iron between the oxidized and the reduced state (Fig. S2) and (iii) the dynamics of characteristics of channels 2, 3, & 4 in high-spin ferric and ferrous *Kp*DyP and the variants D143A, R232A and D143A/R232A (Fig. S3). Supplementary data to this article can be found online at https://doi.org/10.1016/j.jinorgbio.2019.110761.

References

[1] S.J. Kim, M. Shoda, Biotechnol. Bioeng. 62 (1999) 114–119.
[2] M. Zámocký, S. Hofbauer, I. Schaffner, B. Gasselhuber, A. Nicolussi, M. Soudi, K.F. Pirker, P.G. Furtmüller, C. Obinger, Arch. Biochem. Biophys. 574 (2015) 108–119.
[3] R. Singh, L.D. Eltis, Arch. Biochem. Biophys. 574 (2015) 56–65.
[4] V. Pfanzagl, K. Nys, M. Bellei, H. Michlits, G. Mlynek, G. Battistuzzi, K. Djinovic-Carugo, S. Van Doorslaer, P.G. Furtmüller, S. Hofbauer, C. Obinger, J. Biol. Chem. 293 (2018) 14823–14838.
[5] S. Létoffé, G. Heuck, P. Delepelaire, N. Lange, C. Wandersman, Proc. Natl. Acad. Sci. U. S. A. 106 (2009) 11719–11724.
[6] H.A. Dailey, A.N. Septer, L. Daugherty, D. Thames, S. Gerdes, E.V. Stabb, A.K. Dunn, T.A. Dailey, J.D. Phillips, MBio 8 (2011) e00248-11.
[7] M. Ahmad, J.N. Roberts, E.M. Hardiman, R. Singh, L.D. Eltis, T. Bugg, Biochemistry 50 (2011) 5096–5107.
[8] G. Battistuzzi, M. Bellei, C.A. Bortolotti, M. Sola, Arch. Biochem. Biophys. 500 (2010) 21–36.
[9] G. Battistuzzi, M. Bellei, J. Vlasits, S. Banerjee, P.G. Furtmüller, M. Sola, C. Obinger, Arch. Biochem. Biophys. 494 (2010) 72–77.
[10] G. Battistuzzi, M. Bellei, M. Zederbauer, P.G. Furtmüller, M. Sola, C. Obinger, Biochemistry 45 (2006) 12750–12755.
[11] G. Battistuzzi, M. Borsari, L. Loschi, M.C. Menziani, F. De Rienzo, M. Sola, Biochemistry 40 (2001) 6422–6430.
[12] G. Battistuzzi, M. Borsari, A. Ranieri, M. Sola, J. Am. Chem. Soc. 124 (2002) 26–27.
[13] N. Schmid, C.D. Christ, M. Christen, A.P. Eichenberger, W.F. van Gunsteren, Phys. Commun. 183 (2012) 890–903.
[14] N. Schmid, A.P. Eichenberger, A. Choutko, S. Riniker, M. Winger, A.E. Mark, W.F. van Gunsteren, Eur. Biophys. J. 40 (2011) 843–856.
[15] C. Zou, M. Larisika, H. Nagy, J. Strajer, C. Oostenbrink, X. Chen, W. Knoll, B. Liedberg, C. Nowak, J. Phys. Chem. B 117 (2013) 9606–9614.
[16] H. Berendsen, J. Postma, W. Van Gunsteren, J. Hermans, B. Pullman (Ed.), Intermolecular Forces, D. Reidel Publishing Co, Dordrecht, The Netherlands, 1981, pp. 331–342.
[17] H. Berendsen, J. Postma, W.F. Van Gunsteren, A. DiNola, J. Haak, J. Chem. Phys. 81 (1984) 3684–3690.
[18] J. Ryckaert, G. Ciccotti, H. Berendsen, J. Comput. Phys. 23 (1977) 327–341.
[19] H. Berendsen, W. Van Gunsteren, H. Zwinderman, R. Geurtsen, Ann. N. Y. Acad. Sci. 482 (1986) 269–286.
[20] I. Tironi, R. Sperb, P. Smith, W. van Gunsteren, J. Chem. Phys. 102 (1995) 5451–5459.
[21] T. Heinz, W.F. van Gunsteren, P. Hünenberger, J. Chem. Phys. 115 (2001) 1125–1136.
[22] A.P. Eichenberger, J.R. Allison, J. Dolenc, D.P. Geerke, B.A.C. Horta, K. Meier, C. Oostenbrink, N. Schmid, D. Steiner, D. Wang, W.F. van Gunsteren, J. Chem. Theory Comput. 7 (2011) 3379–3390.
[23] E. Chovancova, A. Pavelka, P. Benes, O. Strnad, J. Brezovsky, B. Kozlikova, A. Gora, V. Sustr, M. Klvana, P. Medek, L. Biedermannova, J. Sochor, J. Damborský, PLoS Comput. Biol. 8 (2012) e1002708.
[24] S. Macedo, M. Pechlaner, W. Schmid, M. Weik, K. Sato, C. Dennison, K. Djinović-Carugo, J. Synchrotron Radiat. 16 (2009) 191–204.
[25] S. Mendes, V. Brissos, A. Gabriel, T. Catarino, D.L. Turner, S. Todorovic, L.O. Martins, Arch. Biochem. Biophys. 574 (2015) 99–107.
[26] R. Shresta, G. Huang, D.A. Meekins, B.V. Geisbrecht, P. Li, ACS Catal. 7 (2017) 6352–6364.
[27] G. Battistuzzi, M. Bellei, F. De Rienzo, M. Sola, J. Biol. Inorg. Chem. 11 (2006) 586–592.
[28] G. Battistuzzi, M. Bellei, M. Borsari, G. Di Rocco, A. Ranieri, M. Sola, J. Biol. Inorg. Chem. 10 (2005) 643–651.
[29] A. Ben-Naim, Y. Marcus, J. Chem. Phys. 81 (1984) 2016.
[30] B. Lai, C. Oostenbrink, Theor. Chem. Accounts 131 (2012) 1272.
[31] G. Battistuzzi, M. Bellei, C.A. Bortolotti, G.D. Rocco, A. Leonardi, M. Sola, Arch. Biochem. Biophys. 423 (2004) 317–331.
[32] G. Battistuzzi, J. Stampler, M. Bellei, J. Vlasits, M. Soudi, M. Sola, P.G. Furtmüller, C. Obinger, Biochemistry 50 (2011) 7987–7994.
[33] A. Nicolussi, M. Auer, J. Weissensteiner, G. Schütz, S. Katz, D. Maresch, S. Hofbauer, M. Bellei, G. Battistuzzi, P.G. Furtmüller, C. Obinger, C. Biochemistry 56 (2017) 4525–4538.
[34] A. Nicolussi, J.D. Dunn, G. Mlynek, M. Bellei, M. Zamocky, G. Battistuzzi, K. Djinović-Carugo, P.G. Furtmüller, T. Soldati, C. Obinger, J. Biol. Chem. 293 (2018) 1330–1345.
[35] A. Nicolussi, M. Auer, B. Sevcnikar, M. Paumann-Page, V. Pfanzagl, M. Zámocký, P.G. Furtmüller, C. Obinger, Arch. Biochem. Biophys. 643 (2018) 12–23.
[36] M. Bellei, C. Jakopitsch, G. Battistuzzi, M. Sola, C. Obinger, Biochemistry 45 (2006) 4768–4774.
[37] S. Hofbauer, M. Bellei, A. Sündermann, K.F. Pirker, A. Hagmüller, G. Mlynek, J. Kostan, H. Daims, P.G. Furtmüller, K. Djinović-Carugo, C. Oostenbrink, G. Battistuzzi, C. Obinger, Biochemistry 51 (2012) 9501–9512.
[38] I. Schaffner, G. Mlynek, N. Flego, D. Pühringer, J. Libiseller-Egger, L. Coates, S. Hofbauer, M. Bellei, P.G. Furtmüller, G. Battistuzzi, G. Smulevich, K. Djinović-Carugo, C. Obinger, C. ACS Catal. 7 (2017) 7962–7976.